Article

Characteristics and Connectivity Analysis of Hidden Karst in Jurong Pumped Storage Power Station Area, China

Liqiang Chen [1], Xiaosong Dong [2,*], Kehan Miao [2], Wenjie Yang [2] and Yong Huang [2]

[1] PowerChina Huadong Engineering Corporation Limited, Hangzhou 310014, China; chen_lq@ecidi.com
[2] School of Earth Science and Engineering, Hohai University, Nanjing 211100, China;
miaokh2021@hhu.edu.cn (K.M.); yang_wenjie@hhu.edu.cn (W.Y.); hyong@hhu.edu.cn (Y.H.)
* Correspondence: dongxiaosong@hhu.edu.cn

Abstract: Based on the hidden karst exposed in Jurong Pumped Storage Power Station, combined with the field exploration data, the temporal and spatial development characteristics of hidden karst in the power station area are analyzed using the methods of specific solubility and specific corrosion, water chemical composition analysis, borehole television imaging, tracer test, and water pressure test. The results show that the karst development in the study area can be divided into three periods: pre-Cretaceous, Pleistocene, and modern karst. Karst development is controlled by soluble rock, non-soluble rock, and their combination, and the development direction is basically consistent with the fault strike. Karst caves are mainly distributed below the elevation of 100 m, with different shapes and scales and randomness. Non-soluble rocks and impure carbonate rocks are widely distributed in the study area, and surface karst is not developed. The underground karst caves are filled with red clay, and the rate of groundwater circulation is slow. The existence of geological bodies such as rock veins causes the groundwater levels to have obvious double-layer characteristics, which results in weak connectivity between karst caves. Although the karst in the power station area has a certain hydraulic connection with the surface water outside the area, the hydraulic connection of karst in the power station area is generally weak. The research results provide a scientific basis for the anti-seepage measures of underground powerhouses.

Keywords: hidden karst; development characteristics; connectivity; hydraulic connection

1. Introduction

Large water conservancy and hydropower projects have high requirements for the selection of dam sites. With the increase in large projects, more and more reservoirs are built in karst areas. Karst refers to a unique geological landscape characterized by soluble rocks that can form features such as sinkholes and caves [1]. Hidden karst refers to karst features that are not immediately visible on the surface, such as underground caves and conduits. In hydraulic projects, hidden karst poses challenges such as water inflow, reservoir leakage, and geological disasters. Understanding the characteristics and connectivity of hidden karst is crucial for effective planning and operation of such projects. Various methods, including solubility tests and groundwater analysis, are used to investigate hidden karst and implement measures to reduce its risks. A phased approach involving field surveys, historical mapping, geophysical investigations, and hydrogeological condition analysis is necessary for identifying, investigating, predicting, and reducing sinkhole hazards in karst areas [2]. The existence of karst leads to many problems of water inflow, leakage, and geological disasters [3–5]. Among them, reservoir leakage is the most common problem of reservoirs in karst areas. It has a direct impact on both the storage capacity and power generation capacity of the reservoir. Therefore, if the issue of hidden karst is not adequately addressed, it can significantly affect water storage and subsequently prevent power generation. The investigation of the spatial distribution characteristics and connectivity of karst

caves are crucial to ensure the efficient function of the reservoir and maximize its potential for power generation. For example, Lar Dam has held less than half of its capacity due to the abundance of caves and conduits in the underlying limestone beds and abutments since its construction in 1980 [6]. The leakage has occurred in the Tangab Dam since impounding of the reservoir in 2009 [7].

In order to develop the abundant water conservancy and hydropower resources in these karst areas, it is necessary to solve many special and complex problems caused by karst development, especially the problems of hidden karst. In areas with karst development, especially for pumped storage power station area, the development of karst not only affects the early construction, but also has a huge impact on the later operation. It is necessary to conduct in-depth research on the reservoir karst aquifer system, distribution and formation mechanism, development law and depth, leakage passage, and seepage stability. Various models can be used to describe groundwater flow in karst aquifer systems, including equivalent porous media models [8,9], turbulent conduit flow and diffuse Darcian flow in fine fractures [10], double medium model [11], KAGIS black-box GIS-based model [12], and recharge-discharge semi-distributed model [13]. Zhang, et al. [14,15] integrated petrographic studies, isotope geochemistry, and minor elements to investigate the formation mechanisms and characteristics of karst. Specific solubility and specific corrosion is influenced by the mineral composition in the rock. According to the study on the dissolution mechanism and karst development of carbonate rocks in the karst rocky desertification area of Zhenfeng–Guanling–Huajiang County, Guizhou, China, Bai, et al. [16] found that the dissolution rate of carbonate rocks is positively correlated with the calcite content, while it decreases with increasing content of dolomite. Furthermore, the karst morphology is primarily influenced by the microstructure and mineral assemblage characteristics of carbonate rocks. Zhang, et al. [17] carried out an experimental study and microscopic test to analyze the karst development mechanism and characteristics. According to the study on leakage at the Wanyao dam body, a combined approach of field exploration, hydrochemical analysis, and tracer testing was employed. The objective was to locate water leakage paths at the dam [18]. Qiu et al. [19] employed a new method based on tracer tests to detect and quantify leakage in the Wanyao Dam in Jiangshan City, China. By combining natural tracer tests and an artificial tracer test with salt, the leakage zone of the dam wall can be identified. Isotope tracer test and hydrochemistry monitoring can be used to analyze the recharge and discharge conditions and connectivity of groundwater systems in a karst aquifer [20–23]. Hydrochemical analysis and tracer tests were used to identify the groundwater-leakage mechanism and passage of dams [24–26]. Moreover, electrical resistivity measurements and dye tracer tests were performed to identify the seepage locations [27,28]. Wang et al. [29] have basically identified the development pattern of hidden karst in the foundation of the Cuijiaying Hydroproject on Hanjiang River through methods such as mineralization analysis, borehole television, and water pressure test. Mineralization analysis can identify the solubility of rocks. The borehole TV image can view the geological structure and dissolution of the rock mass inside the hole. Water pressure test can identify the permeability of soluble rocks and indirectly understand the dissolution development and integrity of rock masses. Fang et al. [30] conducted a comprehensive study on the causes of dam leakage and the anti-seepage effect of the anti-seepage curtain using water pressure test, monitoring data, and comprehensive geophysical methods. Seepage effective analysis and seepage control at reservoir sites are fundamental parts of dam design and operations, and the permeability coefficient is the most basic parameter in the seepage analysis of rock mass [31]. In the field test of the karst dam site area, water pressure test is a very essential method to determine the permeability parameters of rock mass; the analysis and calculations were often carried out using the water pressure test [32–35].

These methods have their own applicability, advantages, and disadvantages. It is difficult for any method to fully identify the development characteristics and connectivity of hidden karst in the study area. This research mainly carries out comprehensive analysis by the specific solubility and specific corrosion method, analytical method for chemical

composition of groundwater, television imaging method in borehole, groundwater tracing test, and water pressure test. As the surface karst is not developed in the Jurong Power Station, karst caves and pores mainly develop at an elevation of 0–200 m below the surface (hidden karst). There are underground powerhouses and water diversion tunnels in the area of the hidden karst, and water inflow may occur during construction and operation. Therefore, it is necessary to study the characteristics and connectivity of the hidden karst. The development characteristics and connectivity of hidden karst in the study area were systematically and comprehensively analyzed and investigated. It provides a scientific basis for evaluating the scale of karst leakage and anti-seepage measures of underground powerhouses.

2. Case Study

2.1. Project Overview

Jurong Pumped Storage Power Station (JPSPS) is located in Jurong City, Jiangsu Province, 65 km away from Nanjing City and about 26 km away from Jurong City (Figure 1). The main buildings of the hydroproject are composed of the upper reservoir, the water conveyance system, the underground powerhouses, and the lower reservoir. The installed capacity is 1350 MW. JPSPS is one of the key projects of the 13th Five-Year Plan for Pumped Storage Development of the State Grid Corporation of China. It was approved and replied by the Jiangsu Provincial Development and Reform Commission in May 2016 and officially started construction in March 2017. It is planned to put the first unit into operation at the end of 2024, and all units will be put into operation for power generation in 2025. This article is a study on the exposed hidden karst during the construction and excavation stage of the project.
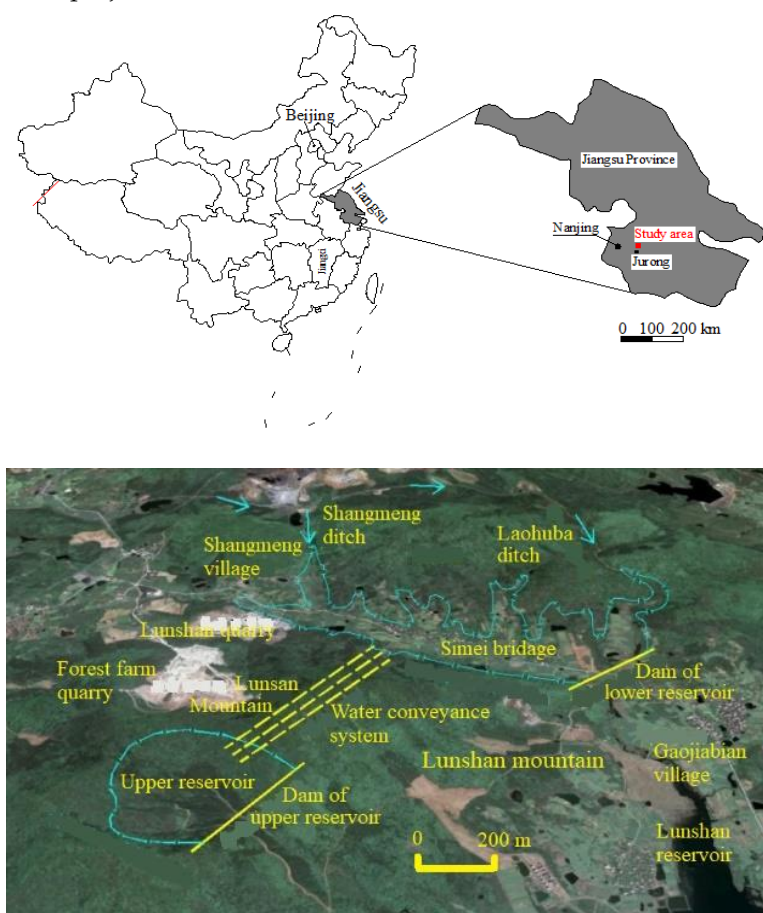

Figure 1. Location of study area.

The upper reservoir is located in the valley on the southwest side of the main peak of Lunshan mountain, with a drainage area of about 0.63 km². The normal storage level of the reservoir is 267.0 m and the dead water level is 239.0 m. The total storage capacity is 17.48 million m³, with an effective storage capacity of 15.77 million m³. The water conveyance system is located in the main peak of Lunshan mountain, with a total length of 1327.89–1363.72 m. The maximum net hydraulic head of the power station is 202 m and the minimum net head is 152 m. The water conveyance system includes the water inlet or outlet of the upper reservoir, the upper horizontal section of the diversion, the diversion surge chamber, the diversion shaft, the lower horizontal section of the diversion, the diversion steel bifurcated pipe and the branch pipe in front of the plant, the tailrace tunnel, and the water inlet or outlet of the lower reservoir. The water inlet or outlet of the upper reservoir is located on the left bank of the upper reservoir, which is the side slope shaft type, and the floor elevation is 220.0 m. The water conveyance system is arranged in a vertical shaft with three tunnels and six turbines. The water inlet or outlet of the lower reservoir is located at the ridge on the right bank of the lower reservoir. The water conveyance system is of a tower type with a side bank slope. The floor elevation is 50.0 m. The size of the underground powerhouse is 246.5 m × 25.5 m × 57.55 m (length, width, and height). The lower reservoir is located in the river section between Simei bridage, Gaojiabian, and Shangmeng villages. The drainage area is 7.75 km² and the water surface of the reservoir is about 2 km long. The normal storage level is 81.0 m and the dead water level is 65.0 m. The total storage capacity is 20.43 million m³ with the effective storage capacity of 16.1 million m³.

2.2. Topographic Features

The study area crosses the main peak of Lunshan mountain from west to east. The top elevation of Lunshan mountain is 400.4 m and the ridge extends about 1.8 km from west to east in general. There is a newly exploited Jurong forest farm quarry on the northwest side of Lunshan mountain (Figure 1). The upper reservoir is located in Dashao valley in the south of Lunshan mountain, with an elevation of 90–110 m. The valley at the dam site is an asymmetric 'V' shape and the reservoir is a basin. The highest point around the reservoir is located in the northeast corner of the reservoir, which is the main peak of Lunshan mountain, with an elevation of 400.4 m. The mountain peak in the west is 375.1 m and the elevation of the narrow mountain pass is 288.30–313.6 m. The southeast side is the gully mouth with the slope of 25–40°. The reservoir basin is uneven, with an elevation of 100–140 m.

The water conveyance system is buried in the Lunshan mountain, passing through the main peak of Lunshan mountain from southwest to northeast. The mountain is relatively wide and thick, with an elevation of 70–400 m. The ridge of Lunshan mountain is gentle. The branch gullies along the pipeline and on both sides are not developed and cut shallow. The inlet or outlet slope of the upper reservoir is slightly steep, with a slope of 30–35°. The inlet or outlet of the lower reservoir is about 15°. The thickness of the upper flat section for the water conveyance is 65–160 m and the lower flat section of the water conveyance is 65–160 m. The overburden rock of bifurcated pipe section is 180–270 m thick and that of underground powerhouse is 95–180 m.

The lower reservoir is located in the north of Lunshan mountain, and the natural reservoir basin is composed of Simei bridge gully and small gully in the north. The Simei bridge gully flows to the southeast. The bottom of the gully is flat, with a ground elevation of 56–82 m. The south reservoir bank is Lunshan mountain. The mountain on the north reservoir bank is wide and gentle. The top elevation of the mountain is 150–226 m. Multiple gullies are developed and the reservoir bank is serrated. The strikes of most ridges are between SN and NWW. The largest branch gully is Laohuba gully in front of the dam, which winds from north to south to the dam site and joins Simei bridge gully at the dam site and then flows into Lunshan reservoir.

In areas with extended karstic phenomena, topography plays a crucial role in influencing karst processes. The unique landforms and features found in karst areas, such as sinkholes, caves, and underground drainage systems, are a direct result of the interaction between groundwater and soluble rock formations. The topographic characteristics, including surface elevation, slope gradient, and drainage patterns, control the distribution and water flow through the karst system and affect groundwater recharge, discharge, and overall hydrological behavior. Understanding the relationship between topography and karst processes is essential for assessing the vulnerability, sensitivity, and management of karst. Groundwater from crystalline rocks is a significant resource in many areas of the world. Stress distributions in fractured rocks control groundwater flow through the evolution of fracture systems, which is influenced by palaeostress and current in situ stress fields [36]. The Samaria Gorge in Crete Island is a prominent geological and geomorphological feature. A comprehensive review of geological models is crucial to understand its evolution due to complex tectonics and stratigraphic uncertainties. Lithological variations, stratigraphy, tectonics, erosion rates, and hydrological conditions contribute to the area's geomorphological evolution [37]. Deep groundwater in fractured crystalline basement is found in deep mines and wells, Stober found that deep thermal waters result from interactions between surface water and rock matrix, as well as mixing with saline deep water [38]. In the upper reservoir and underground powerhouse areas, the elevation difference is relatively large, the terrain slope is steep, the rate of waterflow exchange is fast, and the dissolved carbonate is easily carried away. Therefore, karst is relatively developed in these areas. The terrain of the lower reservoir is relatively flat. The alternation of groundwater circulation is weak and the development of karst is weak.

2.3. Lithology

The exposed lithology in the study area mainly includes Sinian, Cambrian, and Permian strata (Figure 2). Sinian Dengying Group (Z_2dn) is mainly composed of thick bedded fine crystal dolomite and internal clastic dolomite, which are distributed in the lower flat section of water conveyance, underground powerhouse, and tailrace tunnel. The thickness is 150–227 m. Cambrian Guanyintai Group ($\in_{2–3}$gn) is mainly composed of chert-bearing nodules or chert-banded dolomite mixed with argillaceous and calcareous dolomite, which is distributed in the upper horizontal section of the water diversion, the middle and upper parts of the water diversion surge shaft, and the water diversion shaft, with an exposed thickness of 150–210 m. Baotaishan Group ($\in_1$p) is mainly composed of a thin to medium-thin layer of argillaceous dolomite, siliceous dolomite, and cataclastic dolomite, which are distributed from the rear end of the diversion surge shaft to the upper bend of the shaft. The exposed thickness is 39–78 m. The argillaceous dolomite is thin and the surface is strongly weathered. The contact zone and layer are mostly filled with mud. It is a bedding weak interlayer and the contact surface is mainly of rock debris mixed with mud. The upper section of the Mufushan Group ($\in_1$m^2) is mainly composed of phosphorous siliceous rock, phosphorous limestone dolomite, phosphorite, thick bedded, partially thin bedded, etc., which is distributed in the middle lower part of the water diversion shaft to the lower flat section of the water diversion shaft with the thickness of 45–67 m. Permian Longtan Group (P_2l) stratum is mainly composed of carbonaceous mudstone and argillaceous siltstone, distributed at the water inlet or outlet of the lower reservoir, with an exposed thickness of about 100 m. In addition, 31 diorite porphyrite veins (including fault zones) are exposed in the exploratory adit of PD2. The strikes are N40–55° W with dip degrees of 70–90°. The width of diorite porphyrite vein is 0.5–3.0 m. They are in contact with the surrounding rock and are associated with coarse crystal calcite veins. Quaternary eluvial and deluvial clay mixed with gravels is mainly distributed at the toe of both sides, with a thickness of 2–8 m.
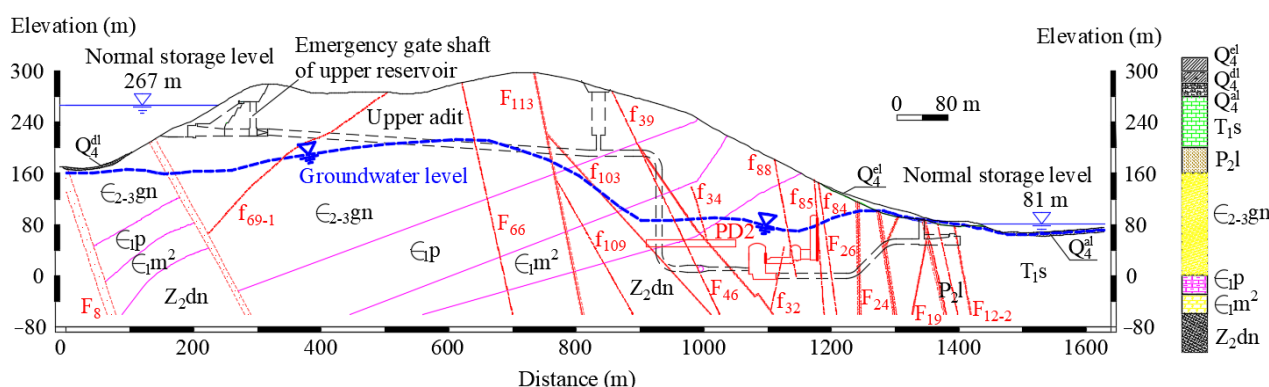
Figure 2. Geological profile map: it shows the spatial distribution of stratigraphic lithology and faults in the study area, as well as the location of the upper reservoir, water transmission pipeline, underground powerhouse, and lower reservoir.

2.4. Geological Structure

The faults in the study area are divided into four groups according to the strikes: (i) NE strike faults, including F_1, F_2, F_3, F_4, F_{5-1}, F_9, and f_1; (ii) NW strike faults, including F_6, F_7, F_8 south segment, and F_{11}; (iii) NNE and NS strike faults, including F_{5-2} and F_8 north segment; and (iv) NWW and EW strike faults, including F_{12-1}, F_{12-2}, F_{10} (Figure 3).
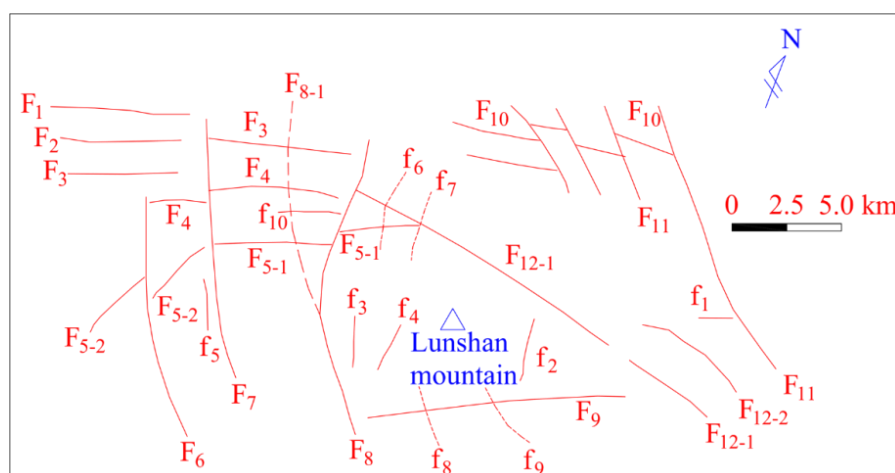

Figure 3. Schematic diagram of relative position and number of faults.

F_8 is a major fault of the upper reservoir, with a length of 14 km and width of 5–10 m. The south end of the upper reservoir is characterized by gullies, which stagger Cambrian strata to the left. There is structural breccia on the north bank, with strong silicification of the rock mass. Diorite porphyrite intrusion can be seen on the surface and in boreholes. Karst caves are developed in the contact zone, with strong rock compression. There are three large faults, F_9, F_{12-1}, and F_{12-2}, in the lower reservoir. Xianrendong fault F_9 is distributed at the southeast slope foot of Lunshan mountain, with a width of 10–15 m, and calcite veins are exposed along the fault. The Simei bridge–Weigang fault F_{12} passes through the left dam foundation of the lower reservoir and shows two parallel faults F_{12-1} and F_{12-2}, of which F_{12-1} is 5–50 m wide. Karst is developed in the contact zone of rock veins, and the boreholes exposed in the fault zone are rich in groundwater. In addition to the above major faults, there are also some smaller faults. Among them, f_1–f_5 are small normal faults, mostly tensile, and f_6–f_9 are inferred shift faults, most of them are torsional or tensile. There is also fault f_{10}, which is located in the quarry of Jurong forest farm. It extends nearly N60° E and the width is more than 10 m, with a dip angle of 75–80° and a length of about 1.2 km. It may be a shift fault.

2.5. Groundwater Types

The groundwater types in the study area mainly include pore water, fracture water, and karst water. Pore water mainly occurs in the brown and yellowish-brown silty clay and clay rubble of the Quaternary Xiashu Group. It has a weak permeability, and the water inflow of a single well is less than 10 m^3/d. The buried depth of groundwater level is 2–5 m, the salinity is less than 1 g/L, and the hydrochemical type is HCO_3-Ca·Na. Fracture water mainly occurs in bedrock fracture and fault zones and can be divided into types of structural and weathering fracture water. The aquifer is recharged by atmospheric precipitation, discharged in the form of spring water, and controlled by the development process of faults and fractures. It is mainly distributed in veins and belts. Karst water plays an important role in the study area. It is developed from weak to medium karst, including karst-fracture water, karst-hole water, and karst-fracture–pipeline water. It is the main groundwater type and mainly recharged by precipitation. Surface water and gully water are also the recharge sources of low-elevation karst water, which is discharged in the form of karst springs.

3. Methods

The comprehensive methods used here mainly include corrosion, chemical composition, television imaging, tracing test, and water pressure test. Among them, solubility, corrosion, and chemical composition are mainly used to analyze the characteristics of hidden karst, while television imaging, tracing test, and water pressure test are mainly used to analyze the connectivity of hidden karst. The use of multiple methods can verify the accuracy of the results.

3.1. Specific Solubility and Specific Corrosion

The chemical composition, mineral composition, and karst development of soluble carbonate rocks are mainly reflected by the correlation between the percentage of CaO and MgO in the soluble rocks and the specific solubility, K_{cv}, which reflects the dissolution intensity of karst, and the specific corrosion, K_v, which reflects the dissolution velocity of karst. The instruments mainly used include thermostatic bath, thermometer, beaker, agitator, filter, Analytical balance, corrosion test tank, potentiometer, pH meter and other conventional experimental instruments. The research results show that the percentage of CaO and MgO in rocks is generally linear with the specific corrosion. The specific solubility and specific corrosion increase with the increase in calcite content in rocks. K_{cv} and K_v can be expressed as:

$$K_{CV} = \frac{\left(C_{CaCO_3} + C_{MgCO_3}\right)/V}{\left(C'_{CaCO_3} + C'_{MgCO_3}\right)/V'} \qquad (1)$$

$$K_V = \frac{(m_0 - m_1)/V}{\left(m'_0 - m'_1\right)/V'} \qquad (2)$$

where K_{cv} represents the specific solubility, C_{CaCO3} is the dissolved amount of sample $CaCO_3$ (mg), C_{MgCO3} is the dissolved amount of sample $MgCO_3$ (mg), C'_{CaCO_3} is the average dissolved amount of standard sample $CaCO_3$ (mg), C'_{MgCO_3} is the average dissolved amount of standard sample $MgCO_3$ (mg), V is the sample volume (cm^3), V' is the average volume of standard sample (cm^3), K_v is specific corrosion, m_0 is the sample mass before dissolution (mg), m_1 is the sample mass after dissolution (mg), m'_0 is the average mass of standard sample before dissolution (mg), and m'_1 is the average mass of standard sample after dissolution (mg). According to K_{cv} and K_v, the solubility sequence of rocks is generally limestone, dolomitic limestone, calcite, marble, calcareous dolomite, and argillaceous dolomite. If the content of calcite is higher than that of dolomite, karst is developed. Moreover, if the content of acid-insoluble substances is high, karst is not developed and, if rocks contain organic matter and asphalt, this is not conducive to karst development.

3.2. Analytical Method for Chemical Composition of Groundwater

In the process of circulation and storage, the groundwater continuously reacts with the surrounding rock mass to form the chemical composition of groundwater, and the chemical composition also undergoes spatiotemporal evolution. In this study, the water quality type and the connectivity characteristics of groundwater are analyzed and judged by the content of main ion components such as Cl^-, SO_4^{2-}, HCO_3^-, Ca^{2+}, Mg^{2+}, Na^+, and K^+. The main testing equipment used is the DZS-706A multi-parameter analyzer produced by Shanghai Reunion Scientific Instrument Co., Ltd. (Shanghai, China).

3.3. Television Imaging Method in Borehole

The basic principle of the borehole digital imaging system is that a special reflective prism imaging CCD optical coupler (HX-JD-04B 3 D intelligent high-definition drilling TV Imager, Wuhan Zhiyan Technology Co., Ltd., Wuhan, China) is used in the downhole equipment to continuously display the image of the borehole walls in 360°, and the computer is used to control the image acquisition and processing. The image processing system automatically collects, unfolds, splices, records, and stores the hole wall images on the computer hard disk and then displays them in 2D or 3D form, that is, converts the annular image taken from the conical reflector into the hole wall unfolded map or histogram. The whole device consists of two parts. The outer part of borehole is mainly composed of computer, controller, winch, foot stand, wellhead pulley, depth sensor, and other hardware. The inner part of borehole is composed of TV camera, light source, reflecting prism, light-transmitting cover, three-axis magnetometer, accelerometer, and focusing device. The two parts are connected by transmission cables for communication. The borehole TV image can provide clear and intuitive videos and pictures and conduct accurate and detailed analysis of lithological data, especially under complex conditions such as lithological fragmentation and karst caves, and it has obvious advantages and good adaptability. This method is employed to detect the spatial distribution characteristics of karst caves.

3.4. Groundwater Tracing Test

Groundwater tracing test is to input some tracers at a certain groundwater point in the upstream (borehole, well, sinkhole, tunnel, etc.) and monitor the presence, time, and concentration of the tracer at the downstream groundwater points, such as spring water, underground powerhouse outlet, and karst underground river outlet, to determine its connectivity. The main testing equipment used is the LTC Levelogger Edge (Model 3001) produced by Solinst Canada Ltd. (Georgetown, ON, Canada). This test is an effective method for studying the specific path of groundwater flow. It is primarily used to investigate the path and speed of karst groundwater, as well as the connection, extension, and distribution of underground river systems. Additionally, it helps to identify the source and channel of mine water inflow, determine the leakage path of reservoirs, and judge the location of groundwater ridges. Furthermore, it can analyze the hydraulic relationships between surface water and groundwater.
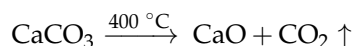
3.5. Water Pressure Test

Water pressure test is a kind of in situ test in which the water pressure is injected into the borehole by means of high pressure, and the fracture development and water permeability of the rock mass are known according to the water absorption calculation of the rock mass. The water pressure test is to isolate a certain length of borehole test section with a special plug and then use a fixed hydraulic head to press water into this section of borehole. The water seeps into the rock body through the fractures around the borehole walls or karst pipes, and the final water volume will tend to a constant value, so as to determine the strength of the rock permeability. It is usually expressed with the permeability, and its unit is Lu value. It is defined as when the water pressure is 1.0 MPa, the water amount is pressed into the rock mass in the per minute and per unit length of the test section.

4. Results

4.1. Karst Development Period

The karst development in the study area mainly undergoes three periods, namely, pre-Cretaceous, Pleistocene, and modern karst. (i) Karst before Cretaceous: the cave is at a high elevation, which is the highest cave in Tangshan and Lunshan area, such as Laohutou cave in the east of Guanyintai, with an elevation of 240.0 m, about 100 m higher than the bottom of the valley. There are thick deposits in the cave, including collapse deposits and Quaternary animal skeleton fossils. (ii) Pleistocene karst: most of the karst development in the study area belongs to this period. Pleistocene brownish-red and brownish-yellow clay is filled in surface karst gullies, karst troughs, and caves. For example, TC8 trench revealed that Xiashu soil (Q_{3x}) was more than 5 m thick, which is the product of karst in this period. (iii) Modern karst: it is characterized by the exposed karst spring water, and there is a trace gas overflowing from the spring water. The gas composition is CO_2. According to the analysis of the gas sources, it is believed that the CO_2 gas is released by the thermal metamorphism of the deep Xujiashan–Jinzishan overthrust, and its reaction formula can be expressed by:

$$CaCO_3 \xrightarrow{400\ ^\circ C} CaO + CO_2 \uparrow$$

Most of the karst in the study area belongs to Pleistocene karst. Owing to the weak permeability of the deposits and clay in the cave, the connectivity of karst caves and pores is very weak.

4.2. Karst Solubility

Lithology and its combination are the main factors that restrict the development of karst. Lithology characteristics, differences in chemical composition of rocks, especially the changes in composition of limestone and dolomite, and the thickness of argillaceous matter are the important preconditions that affect the development of karst and determine the solubility of rocks.

The main index of carbonate rock solubility, specific solubility or specific corrosion, increases with the increase in calcite content and decreases with the increase in dolomite content. The dolomite content in the Cambrian Guanyintai Group strata can reach 60–90% or even more, and the calcite content is only 5–40%. According to the chemical characteristics of soluble rocks in the study area, the lithology is mainly dolomitic limestone, calcareous dolomite, and dolomite, so the karst development is very weak. From the perspective of specific corrosion, the solubility of Guanyintai Group rock stratum, which represents dolomite rock stratum, is worse than that of limestone of other formations. The value of specific corrosion depends on the ratio of CaO and MgO in the rock. The CaO/MgO values of the dolomite of the Sinian Dengying Formation and the Cambrian Guanyintai Group in the area is only 2.08–2.84, which is relatively weak in solubility. The solubility of Sinian dolomite, Cambrian siliceous dolomite, and other pure dolomite formations in the underground area is slightly weak, and the solubility of impure carbonate formations is the worst.

The rock strata in the study area are divided into two major categories: soluble rock and non-soluble rock formations. The Silurian, Devonian, Jurassic, Cretaceous, and Tertiary and Quaternary strata are all non-soluble rocks. According to the solubility and corrosion difference of the rock formation, the soluble rock formation can be divided into pure and impure carbonate rock. The pure carbonate rock formation is mainly composed of limestone and dolomite. It has uniform lithology, large thickness, and relatively developed corrosion. The representative lithology is mainly sparry arenaceous limestone of the Ordovician Honghuayuan formation, limestone of the Permian Qixia and Triassic Qinglong formations, and the breccia limestone of Zhouchongcun formation. Karst is not developed in non-soluble rock layer and impure carbonate rock, and the representative lithology is Sinian Dengying dolomite, Cambrian Guanyintai Group dolomite, and Permian Tan carbonaceous mudstone and shale. Therefore, as non-soluble and impure carbonate rocks

are widely distributed in the study area, the karst in the study area is not developed and its connectivity is weak.

4.3. Fault and Karst

The geological structure directly affects the scale and intensity of karst development and controls the direction and pattern of karst development. The study area is the core of the east end of Tanglun anticline, with an axial direction of nearly N60° E. The north side is a noncarbonate formation, and the south outer edge is also a noncarbonate formation. The NW trending faults and fractures are important factors controlling the development of karst. The rose diagrams are made for fault, rock, and karst fractures in the study area (Figure 4). It can be seen from the diagram that the direction of the most karst fractures is basically consistent with the strikes of faults and fractures.

Figure 4. Rose diagrams of the strikes: it shows that the development direction of karst fractures is basically consistent with the direction of rock fractures and faults, indicating that the development of hidden karst is controlled by faults and fractures.

The main faults that have important influence on karst development are F_8, F_{12-1}, F_{13}, F_7, F_{71}, F_{72}, etc. The fault F_8 extends from the bottom of the upper reservoir trench through the dam site and the northern reservoir bank, and diorite porphyrite intrudes. It is a compressive torsional fault. Boreholes ZK4, ZK9, ZK58, and ZK84 are arranged along the fault to expose karst caves (Figure 5). The other boreholes have developed corrosion fractures. Borehole ZK4 discloses a karst cave with a vertical width of 0.8 m and an elevation of 52.03 m, and the sediment in the cave has been calcified. Borehole ZK9 exposes a karst cave with a vertical width of 8.4 m and an elevation of 44.46 m, which is filled with red clay and calcite veins in the cave. Borehole ZK58 exposes a karst cave with a vertical diameter of 2.9 m and an elevation of 96.02 m, which is filled with red clay. At the elevation of 71.29–43.67 m, borehole ZK84 exposes four karst caves with a diameter of 1.6–15.1 m, which are mostly filled with red clay.

Fault F_{13} extends from the bottom of the upper reservoir to the outside of the reservoir through the northeast reservoir bank. The diorite porphyrite vein intrudes into the fault zone. Three boreholes, ZK22, ZK67, and ZK115, are exposed to karst caves, among which borehole ZK22 exposes a 7.5 m wide karst cave at an elevation of 184.77 m, which are filled with clay. Borehole ZK67 exposes a karst cave with a diameter of 2.7 m and an elevation of 172.12 m. Borehole ZK115 exposes a 1.0 m diameter karst cave and an elevation of 83.17 m. Fault F_{12-1} runs through the lower reservoir at the foot of the north slope of Lunshan mountain and the Simei bridge gully. The footwall of the fault zone is composed of soluble rocks, while the soluble and non-soluble rocks are staggered in the hanging wall. Boreholes ZK24, ZK105, ZK110, ZK145, and ZK148 arranged on both sides reveal karst caves or small karst holes. Faults F_{71} and F_{72} pass through Qinglong limestone, and karst fractures and caves are developed in the fault zone. Along the fault F_7, the rock mass in the affected zone

is broken and has good permeability, so karst dry valley is developed along the fault zone. There is one 3.9 m karst cave exposed in borehole ZK80.

(**a**)   (**b**)

Figure 5. Karst caves and fillings exposed by boreholes in the fault F$_8$: (**a**) clay filling of karst cave with a depth of 18.1–21.0 m in the borehole ZK58 and (**b**) clay filling of karst cave with a depth of 49.5–58.3 m in the borehole ZK84.

The above analysis shows that the karst development direction is basically consistent with the fault strike. At the same time, several faults and fault zones in the study area have exposed karst caves, which are discontinuous and vary in sizes and scales, and some karst caves are filled with red clay. Therefore, the karst or karst caves developed along the faults have a certain degree of connectivity.

4.4. Elevation Characteristics of Karst Development

The distribution elevation of karst phenomena exposed in the study area, such as corrosion fractures, karst caves, karst gullies, butterfly pits, and karst dry valleys, is statistically analyzed (Figure 6). It can be seen from Figure 6 that the highest elevation of karst caves is 274.07 m, the lowest elevation is −17.71 m, the karst caves below the elevation of 100.0 m are relatively concentrated, and the karst caves above the elevation of 140 m are relatively scattered. The elevation of karst development is related to the elevation of stratigraphic distribution. The distribution of karst in the dolomite strata of Guanyintai, Dengying, Paotai Mountain, and Mufu Mountain groups varies greatly from 17 to 174 m. Limestone strata of Qinglong, Honghuayuan, Lunshan, Qinglong, Qixia, and Zhouchongcun groups are generally developed below the elevation of 100 m. Therefore, the surface karst in the study area is not developed, and the karst and karst caves are mainly distributed under the ground (hidden karst).
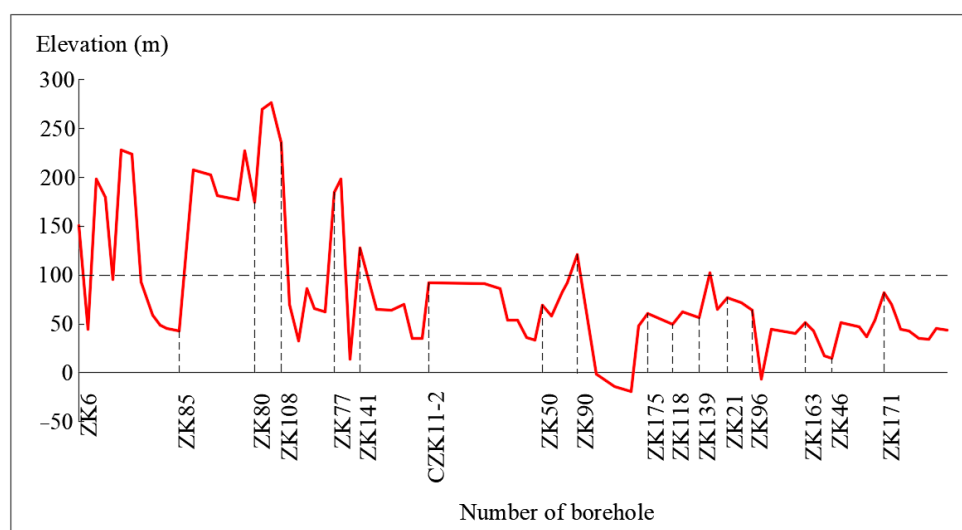

Figure 6. Elevation distribution characteristic of exposed karst caves in different boreholes.

According to the comprehensive analysis of TV imaging in the boreholes, five large karst caves are currently developed in the underground powerhouse. The karst cave LD1 is exposed at the right of the upstream side wall with a stake number of 0 + 92–0 + 97 m and an elevation of 40–45 m. LD2 is exposed at the right of the upstream side wall with a stake number of 0 + 90–0 + 100 m and an elevation of 35.5–46.0 m. LD3 is exposed at the right of the plant with a stake number of 0 + 115–0 + 126 m and an elevation of 31.0–46.0 m. LD4 is exposed at the right of the plant with a stake number of 0 + 133–0 + 1142 m and an elevation of 31.0–42.0 m. LD5 is exposed at the right of the plant with a stake number of 0 + 144–0 + 147 m and an elevation of 36.0–43.0 m. The karst caves are filled with red clay in soft plastic shape. The distribution of karst caves is shown in Figure 7. Therefore, according to the elevation of karst development, karst and karst caves in the study area are mainly distributed under the ground (hidden karst) with different scales and shapes, and the distribution position is random. A small number of karst caves have certain hydraulic connection through faults, such as LD2 and LD3, which are connected by f_{37}, and the connection between most karst caves is relatively weak.
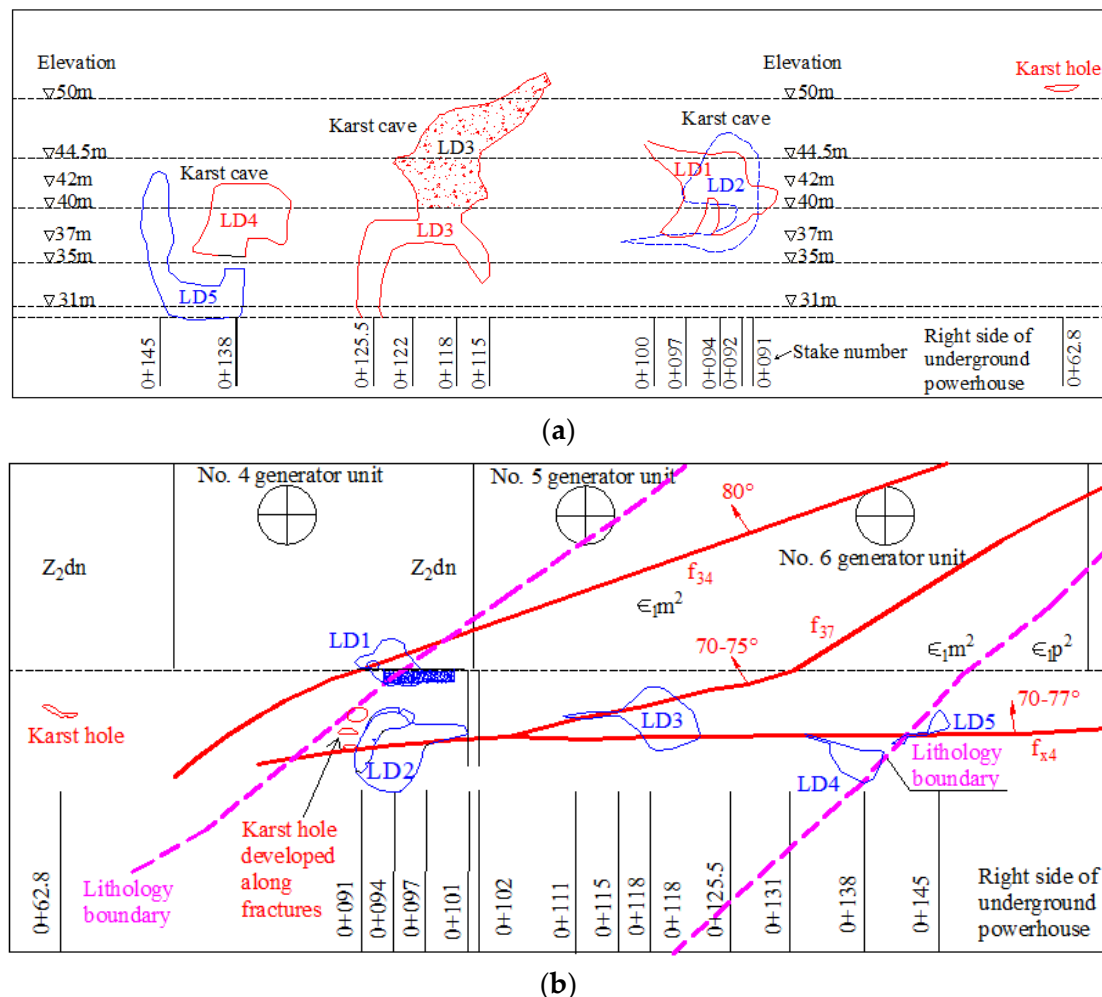

(a)

(b)

Figure 7. Spatial distribution map of karst caves: (**a**) vertical distribution of karst cave on upstream side wall and (**b**) plane section of karst cave at elevation 42 m.

4.5. Characteristics of Karst Groundwater

According to the results of water quality analysis, the hydrochemical types are generally divided into three types: (i) HCO_3-Ca·Mg type, which is mainly distributed in the aquifer of dolomite and dolomitic limestone from the Cambrian Guanyintai Group of the upper reservoir and the Lower Ordovician Lunshan Group. Milligram equivalent ratio of

Ca/Mg is close to 1.0. (ii) HCO$_3$-Ca type, which is distributed in the limestone strata of Ordovician Honghuayuan, Permian Qixia, Gufeng, Yanqiao, and Triassic Qinglong groups. Milligram equivalent ratio of Ca/Mg is more than 2.0. (iii) SO$_4$-Ca type, where the content of Ca^{2+} in groundwater has little change, which is about 80–90 mg/L. The content of Mg^{2+} in dolomite area is 30–40 mg/L, while the value in limestone area is less than 10 mg/L. The hardness of groundwater, which is the sum of the milligram equivalents of Ca^{2+} and Mg^{2+}, is 4.51–8.43 mg/L, most of which is greater than 5 mg/L. The hardness is relatively high, which indicates that the groundwater alternates slowly. Therefore, the study area is mainly a solution-fracture aquifer system, and there is no vein or pipeline flow. The large difference of groundwater quality also reflects that the karst in the study area is not closely related, but there is a certain hydraulic connection between the local karsts.

4.6. Double-Layer Water Level and Karst

The karst aquifer system in the study area has the following characteristics: (i) it is the karst-fracture aquifer with large thickness; (ii) due to the existence of rock vein, the variation in groundwater level is great and there is a water drop phenomenon; (iii) controlled by the discharge datum level, the groundwater forms the discharge characteristics of multiple layers; and (iv) the water pressure test shows that the water level in the borehole decreases with the increase in the borehole depth and the Lu value changes discontinuously with depth. Taking borehole ZK21 as an example, the Lu value of water pressure test shows characteristics of two layers as a whole along with the depth. The permeability of the formation above the elevation of 85 m is discontinuous, and there are at least two relative aquicludes. The permeability of the formation below 85 m has little change, and the Lu value is about 5–6. At the same time, due to the existence of the relative aquiclude, the measured groundwater levels during the water pressure test also reflect that the levels occur at the characteristics of multiple layers and the depths completely correspond with the levels (Figure 8). The appearance of double water level makes the deep groundwater mainly in a stagnant state, and the runoff and circulation of groundwater is very slow. Moreover, the supply of shallow water to deep water is limited. The above analysis shows that the groundwater level has obvious double-layer characteristics due to the existence of geological bodies such as rock veins. Therefore, the karst development is discontinuous in the vertical direction, and the hydraulic connection is relatively weak.
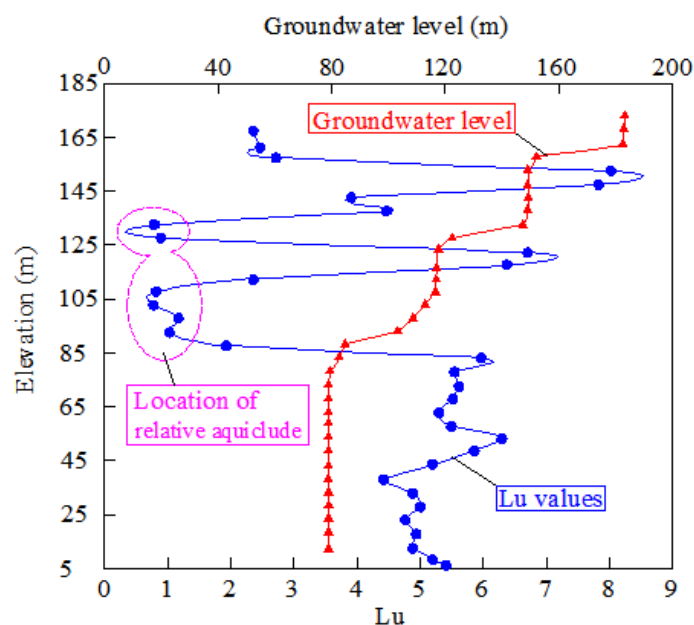

Figure 8. Lu value and groundwater level change in borehole with the depth ZK21 during the water pressure test.

4.7. Characteristics of Karst Leakage and Ecological Impact

The karst system, known for its complexity, sensitivity, vulnerability, and ecological value, faces potential risks associated with the construction of hydroelectric power plants (HEPP) and grout curtains [39]. Grout curtains are commonly used in karst areas to reduce water loss from reservoirs. A study conducted on the Prevoj dam in western Serbia employed long-term and short-term water level monitoring to assess the hydraulic behavior and effectiveness of grout curtains [40]. Additionally, the exploitation of reservoirs for water energy has gained attention due to the depletion of traditional energy sources. However, the interaction between nutrients and hydrological conditions in karst areas often leads to water quality issues [41].

Due to the certain scale of hidden karst in the research area, there is a possibility of leakage from the upper water reservoir to the underground powerhouse. The main cavities of the underground powerhouse are located below the groundwater level. During the construction process, there are leaky and dripping phenomena along faults and fractures, and short-term water inflow phenomena may occur locally. The leakage will gradually decrease with time and tend to stabilize, resulting in a certain impact on the groundwater environment in the short term. The anti-seepage and drainage measures for the underground powerhouse should be strengthened. After the excavation of underground caverns, it may cause a decrease in the local groundwater level along the water transmission pipeline and form a new groundwater discharge reference plane or cone of depression near the excavation bottom plate. After the completion of construction, the anti-seepage measures of the project will be implemented and begin to play an important role. The groundwater around the tunnels will soon recover to a new dynamic equilibrium, owing to various recharges. Therefore, although excavation during construction may lower the groundwater level within a certain range, it has little impact on the ecological environment, such as groundwater, surface water, and vegetation in the study area.

4.8. Tracer Tests and Karst

4.8.1. Tracer Tests in Underground Powerhouse

The tracing test is mainly to find out the hydraulic connection between the karst water and groundwater in the powerhouse area. During the period of the tests, salt and bright blue tracers are used. The tracer injection point was arranged at the middle of drainage gallery C3-4 with a stake number of 0 + 45.6 m and an elevation 21.4 m (Figure 9). The receipt point was at the lower drainage gallery C4-3 with a stake number of 0 + 68.5 m and an elevation of 1.0 m, where the water volume at the receipt point is about 3 L/s. The receipt point is located in Mufushan Group ($\in_1 m^2$) and fault F_{97}. The fault strike is N20° W, with a dip angle of 85–90°. There are cataclastic rocks and a small amount of fault gouge in the fracture zone, and the width of the fracture zone is 1–3 m. During the tracer test, the observation frequency is 10–20 min and the total observation time is about 4 h. The change in water temperature is 16.9–17.3 °C and the conductivity change is 630–640 μs/cm. No peak value of conductivity is detected at the receipt point (Figure 10) and no bright blue tracer is found. The distance between the receipt point and the injection point is about 290 m, the elevation difference is 20.4 m, and the hydraulic gradient is about 0.07. Therefore, it can be judged that there is no obvious hydraulic connection between the injection point (C3-4) and the receipt point (C4-3).
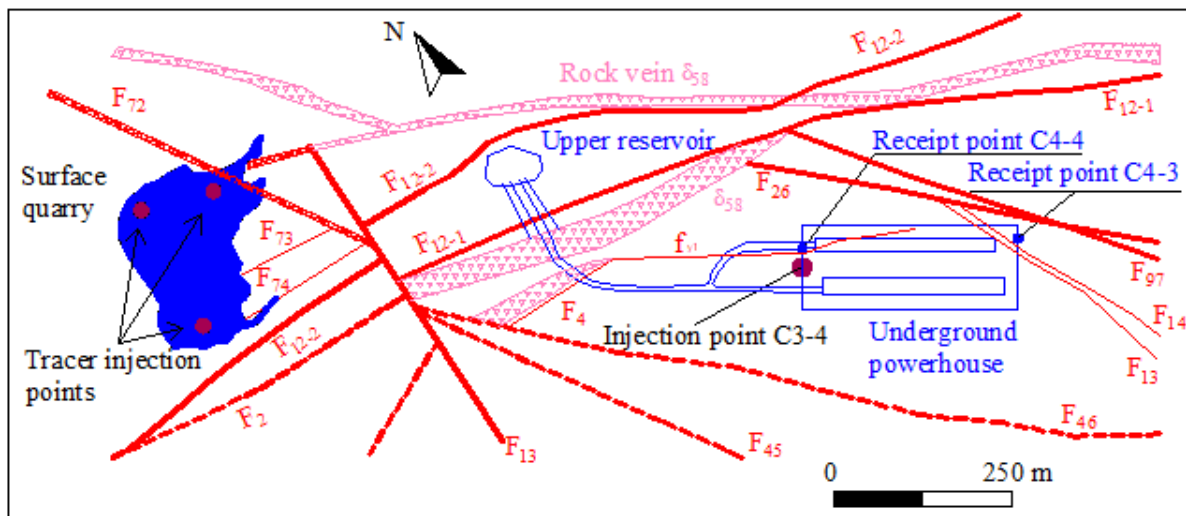
Figure 9. Location of source injection and receipt points for tracer tests in underground powerhouse area.
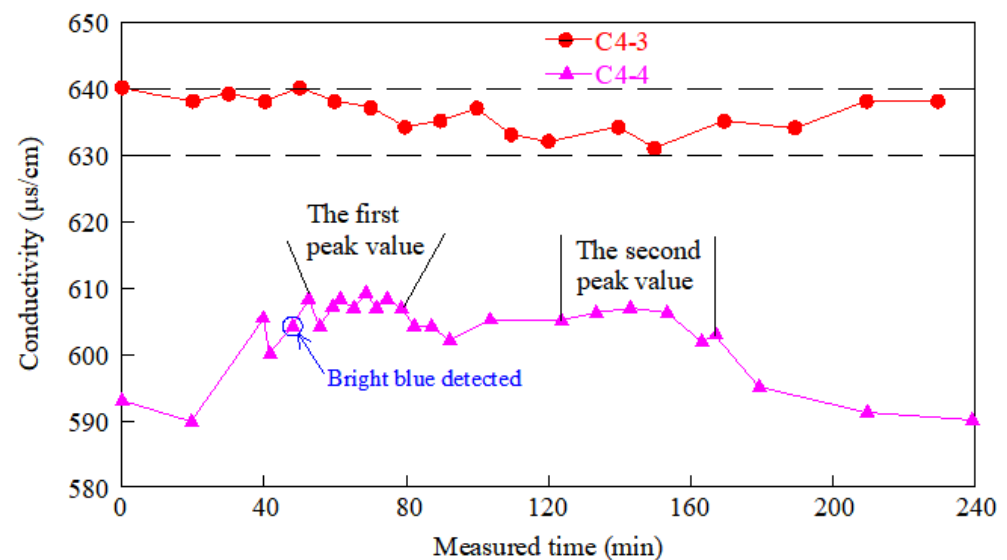

Figure 10. Change curves of conductivity with time.

Moreover, another receipt point was at the lower drainage gallery C4-4 with a stake number of 0 + 55.0 m and an elevation of −5.5 m, and the water volume at the receipt point is about 100 m^3/h. During the tracer test, the observation frequency is 3–20 min and the total observation time is about 4 h. The change in water temperature is 16.4–16.5 °C and the conductivity change is 590–609 μs/cm. The peak value of conductivity was detected at the receipt point (Figure 10). The bright blue tracer was observed about 27 min after the tracer source was injected (Figure 11), and the conductivity also changed obviously. The horizontal distance between the receipt point and the injection point was 9.4 m, the elevation difference was 26.4 m, and the hydraulic gradient was about 2.8. Therefore, it can be judged that there is obvious hydraulic connection between the injection point (C3-4) and the receipt point (C4-4). In addition, it can be seen from Figure 10 that two conductivity peak values were monitored during the test, and the first peak value was higher than the second peak, which indicates that there may be two fracture-karst passages between the receipt and injection points.
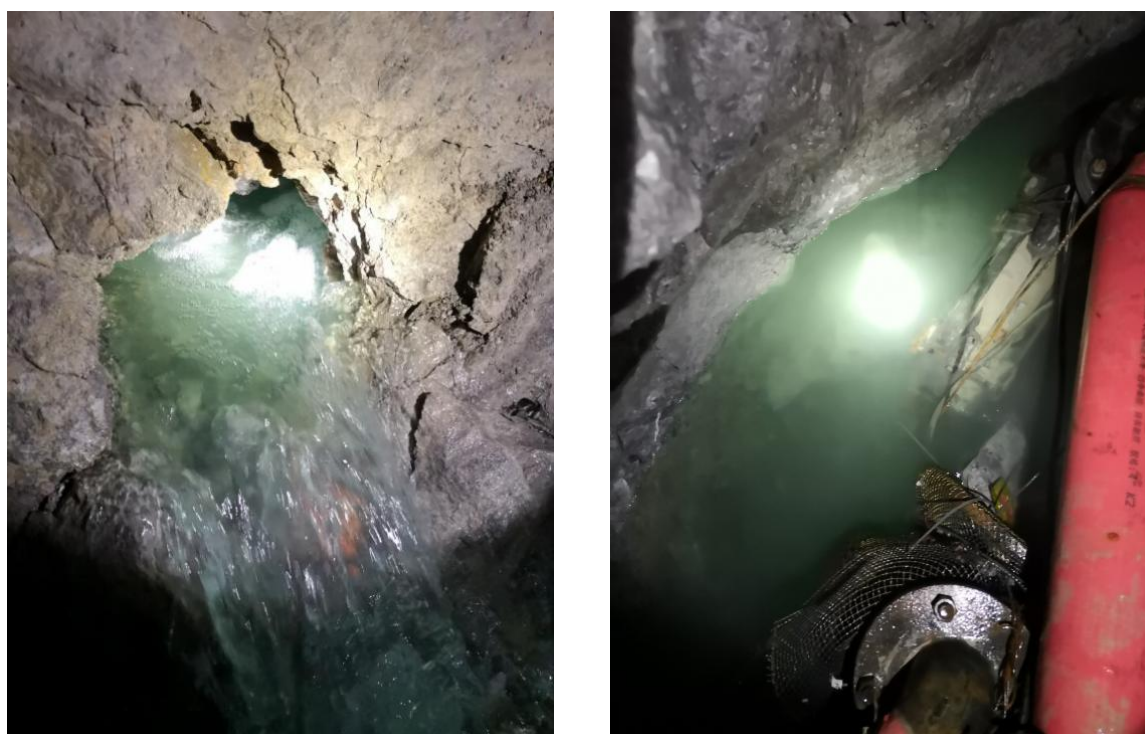
Figure 11. Bright blue tracer observed at the receipt point C4-4.

4.8.2. Tracer Test in Underground Powerhouse and Its Surroundings

The injection point of this test is located in the surface quarry on the west side of the powerhouse, with a straight-line distance of about 800 m from the powerhouse and an elevation of 100 m. Two kinds of tracers are used, including 50 kg of salt tracer and 500 g of brilliant blue tracer. Since the quarry is relatively large, the time of source injection is about 1 h and 15 min. There are two receipt points, which are, respectively, the outlet points of the lower drainage galleries C4-3 and C4-4. The observation time of lower drainage gallery C4-3 is about 5 h, with an observation frequency of 5 min. The observation time of the lower drainage gallery C4-4 is about 5 h, with an observation frequency of 1 min.

The background value of conductivity is 660–670 μs/cm. The measured maximum conductivity is 725 μs/cm. It shows a large difference from the background value and indicates that the tracer from the source injection point has been received. Multiple peak values of conductivity are received during the test, the first maximum peak of which is 723 μs/cm received at 13:00, and the second maximum peak is 725 μs/cm received at 16:40 (Figure 12), which may be related to the complex underground fault network. There are multiple paths from the source injection point to the receipt point. The earliest change time of the conductivity for this receipt point is 12:48. Compared with the time of the source injection, the migration time of the tracer from the source injection point to the receipt point is about 1 h and 15 min to 2 h and 33 min.

The curve of conductivity change with time at the receipt point C4-4 of the lower drainage gallery is shown in Figure 12, where the background value of conductivity is about 300–330 μs/cm and the maximum conductivity measured in the test is 508 μs/cm, which indicates that the tracer has been received. During the test, about five peak values were received, and the 'tailing' phenomenon after each peak value was obvious. This infers multiple paths from the source point to the receipt point. The earliest change in time of the conductivity for this receipt point is 12:23. Compared with the source injection time, the migration time of the tracer is about 53 min to 2 h and 8 min. Therefore, the lower drainage gallery C4-4 receives the tracer 26 min earlier than that the lower drainage gallery C4-3 receipt point.
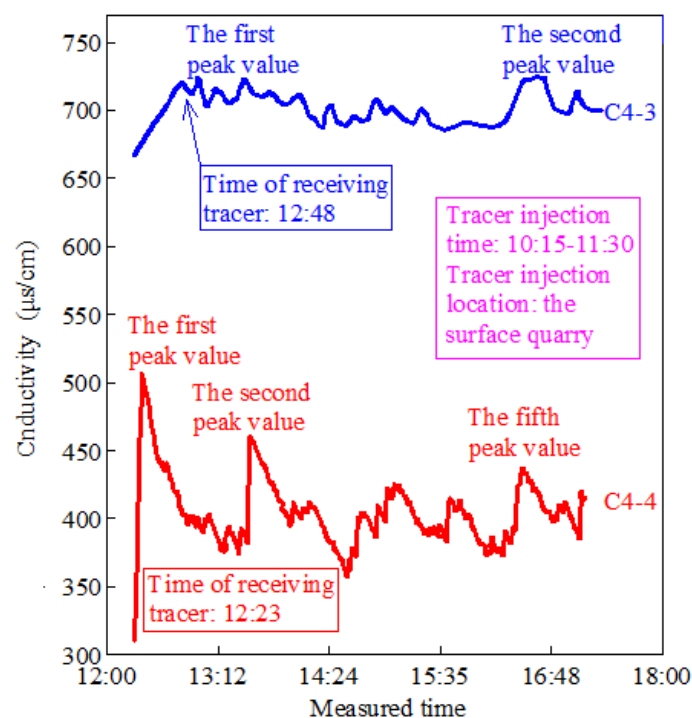
Figure 12. Change curves of conductivity with time: receipt point for lower drainage gallery C4-3 and receipt point for lower drainage gallery C4-4.

According to the test data analysis of the two receipt points, the surface water in the quarry on the west side of the powerhouse is closely hydraulically related to karst water in the powerhouse area.

5. Discussion and Conclusions

Karst often develops along various fault zones and forms large-scale karst channels, affecting the normal operation of reservoirs. Based on the comprehensive analysis of landform, lithology, geological structure, chemical composition of soluble rock, chemical composition of groundwater, and relevant field tests, it is determined that the karst development of JPSPS has the following characteristics.

Karst development is controlled by lithology and geological structure. It is mainly developed in pure carbonate. The surface karst is not developed, while underground hidden karst is dominant. The intensity of karst development is closely related to the geological structure, and the development direction of corrosion fracture is basically consistent with the strike of faults and fractures, which is mainly developed along the rock layer and the NW and NE directions. No large-scale underground rivers and other karst phenomena are found.

The connectivity of karst development is relatively weak. Because most of the karst caves are filled with red clay, the connectivity in the karst caves is very weak. Except for the karst caves developed along the fault, the connectivity between most karst caves is very weak. The existence of double-layer water level also shows that the vertical connectivity of karst is relatively weak. There is a certain hydraulic connection between the surface water around the powerhouse and the karst water in the powerhouse area.

Due to the relatively developed hidden karst in the underground powerhouse area, there is a possibility of water inflow. Therefore, timely drainage should be paid attention to during construction. After the construction is completed, the underground tunnels should be lined in a timely manner and the underground powerhouse should be promptly impermeable to reduce the leakage from the upper reservoir during the operation of the reservoir.

References

1. Nazik, L.; Poyraz, M.; Karabıyıkoğlu, M. Karstic landscapes and landforms in Turkey. In *Landscapes and Landforms of Turkey*; Springer: Cham, Switzerland, 2019; pp. 181–196.
2. Gutierrez, F.; Cooper, A.H.; Johnson, K.S. Identification, prediction, and mitigation of sinkhole hazards in evaporite karst areas. *Environ. Geol.* **2008**, *53*, 1007–1022. [CrossRef]
3. He, K.Q.; Yu, G.M.; Lu, Y.R. Palaeo-karst collapse pillars in northern China and their damage to the geological environments. *Environ. Geol.* **2009**, *58*, 1029–1040. [CrossRef]
4. Zhao, Y.D.; Shi, Y.; Wu, F.H.; Sun, R.; Feng, H. Characterization of the sinkhole failure mechanism induced by concealed cave: A case study. *Eng. Fail. Anal.* **2021**, *119*, 105017. [CrossRef]
5. Liu, Y.; Zhu, J.Z.; Liu, Q.M.; Yuan, A.Y.; He, S.F.; Bai, Y.S. Mechanism Analysis of Delayed Water Inrush from Karst Collapse Column during Roadway Excavation Based on Seepage Transition Theory: A Case Study in PanEr Coal Mine. *Energies* **2022**, *15*, 4987. [CrossRef]
6. Uromeihy, A. The Lar Dam; an example of infrastructural development in a geologically active karstic region. *J. Asian Earth Sci.* **2000**, *18*, 25–31. [CrossRef]
7. Mozafari, M.; Milanovic, P.; Jamei, J. Water leakage problems at the Tangab Dam Reservoir (SW Iran), case study of the complexities of dams on karst. *Bull. Eng. Geol. Environ.* **2021**, *80*, 7989–8007. [CrossRef]
8. Pankow, J.F.; Johnson, R.L.; Hewetson, J.P.; Cherry, J.A. An evaluation of contaminant migration patterns at two waste disposal sites on fractured porous media in terms of the equivalent porous medium (EPM) model. *J. Contam. Hydrol.* **1986**, *1*, 65–76. [CrossRef]
9. Scanlon, B.R.; Mace, R.E.; Barrett, M.E.; Smith, B. Can we simulate regional groundwater flow in a karst system using equivalent porous media models? Case study, Barton Springs Edwards aquifer, USA. *J. Hydrol.* **2003**, *276*, 137–158. [CrossRef]
10. Atkinson, T.C. Diffuse flow and conduit flow in limestone terrain in the Mendip Hills, Somerset (Great Britain). *J. Hydrol.* **1977**, *35*, 93–110. [CrossRef]
11. Robineau, T.; Tognelli, A.; Goblet, P.; Renard, F.; Schaper, L. A double medium approach to simulate groundwater level variations in a fissured karst aquifer. *J. Hydrol.* **2018**, *565*, 861–875. [CrossRef]
12. Valdes-Abellan, J.; Pardo, M.A.; Jodar-Abellan, A.; Pla, C.; Fernandez-Mejuto, M. Climate change impact on karstic aquifer hydrodynamics in southern Europe semi-arid region using the KAGIS model. *Sci. Total Environ.* **2020**, *723*, 138110. [CrossRef] [PubMed]
13. Ollivier, C.; Mazzilli, N.; Olioso, A.; Chalikakis, K.; Carriere, S.D.; Danquigny, C.; Emblanch, C. Karst recharge-discharge semi distributed model to assess spatial variability of flows. *Sci. Total Environ.* **2020**, *703*, 134368. [CrossRef] [PubMed]
14. Zhang, H.T.; Xu, G.Q.; Zhan, H.B.; Zheng, J.B.; Wang, M.H.; Liu, M.C.; Pan, S.Q.; Wang, N. Formation mechanisms of paleokarst and karst collapse columns of the Middle Cambrian-Lower Ordovician carbonates in Huainan coalfield, Northern China. *J. Hydrol.* **2021**, *601*, 126634. [CrossRef]
15. Zhang, H.T.; Xu, G.Q.; Zhan, H.B.; Li, X.; He, J.H. Simulation of multi-period paleotectonic stress fields and distribution prediction of natural Ordovician fractures in the Huainan coalfield, Northern China. *J. Hydrol.* **2022**, *612*, 128291. [CrossRef]
16. Bai, Y.E.; Liu, Q.; Gu, Z.F.; Lu, Y.R.; Sheng, Z.P. The dissolution mechanism and karst development of carbonate rocks in karst rocky desertification area of Zhenfeng-Guanling-Huajiang County, Guizhou, China. *Carbonate Evaporite* **2019**, *34*, 45–51. [CrossRef]
17. Zhang, K.N.; Zhu, K.F.; He, Y.; Zhang, Y.Y. Experimental study on karst development characteristics of calcrete and analysis of its dissolution mechanism. *Carbonate Evaporite* **2022**, *37*, 41. [CrossRef]
18. Huang, Y.; Hou, X.L.; Fu, Z.M.; Wang, J.G. Detection of leakage paths at the Wanyao dam body in Southwest China by hydrochemical analysis and tracer testing. *Environ. Earth Sci.* **2018**, *77*, 791. [CrossRef]
19. Qiu, H.Y.; Hu, R.; Huang, Y.; Gwenzi, W. Detection and Quantification of Dam Leakages Based on Tracer Tests: A Field Case Study. *Water* **2022**, *14*, 1448. [CrossRef]

20. Barbieri, M.; Boschetti, T.; Petitta, M.; Tallini, M. Stable isotope (2H, 18O and 87Sr/86Sr) and hydrochemistry monitoring for groundwater hydrodynamics analysis in a karst aquifer (Gran Sasso, Central Italy). *Appl. Geochem.* **2005**, *20*, 2063–2081. [CrossRef]

21. Jang, J.; Lee, J.Y.; Kim, H. Characteristics of Hydrochemistry and Stable Isotopes in a Karst Region in Samcheok, Republic of Korea. *Water* **2021**, *13*, 213. [CrossRef]

22. Palcsu, L.; Gessert, A.; Turi, M.; Kovacs, A.; Futo, I.; Orsovszki, J.; Puskas-Preszner, A.; Temovski, M.; Koltai, G. Long-term time series of environmental tracers reveal recharge and discharge conditions in shallow karst aquifers in Hungary and Slovakia. *J Hydrol. Reg. Stud.* **2021**, *36*, 100858. [CrossRef]

23. Wang, Z.J.; Guo, X.L.; Kuang, Y.; Chen, Q.L.; Luo, M.M.; Zhou, H. Recharge sources and hydrogeochemical evolution of groundwater in a heterogeneous karst water system in Hubei Province, Central China. *Appl. Geochem.* **2022**, *136*, 105165. [CrossRef]

24. Peng, T.R.; Wang, C.H. Identification of sources and causes of leakage on a zoned earth dam in northern Taiwan: Hydrological and isotopic evidence. *Appl. Geochem.* **2008**, *23*, 2438–2451. [CrossRef]

25. Vasic, L.; Milanovic, S.; Puskas-Preszner, A.; Palcsu, L. Determination of the groundwater-leakage mechanism (binary mixing) in a karstic dam site using thermometry and isotope approach (HPP Visegrad, Bosnia, and Herzegovina). *Environ. Earth Sci.* **2020**, *79*, 174. [CrossRef]

26. Noraee-Nejad, S.; Sedghi-Asl, M.; Parvizi, M.; Shokrollahi, A. Salt tracer experiment through an embankment dam. *IJST-Trans. Civ. Eng.* **2021**, *45*, 2787–2797. [CrossRef]

27. Al-Fares, W. Contribution of the geophysical methods in characterizing the water leakage in Afamia B dam, Syria. *J. Appl. Geophys.* **2011**, *75*, 464–471. [CrossRef]

28. Yilmaz, S.; Koksoy, M. Electrical resistivity imaging and dye tracer test for the estimation of water leakage paths from reservoir of Akdegirmen Dam in Afyonkarahisar, Turkey. *Environ. Earth Sci.* **2017**, *76*, 829. [CrossRef]

29. Wang, Q.; Lin, S.; Wu, S.; Huang, H.; Ding, S. Hidden karst in dam foundation of Cuijiaying Hydroproject on Hanjiang River. *Chin. J. Geotech. Eng.* **2010**, *32*, 1772–1779.

30. Fang, Y.; Li, Z.; Fan, G.; Jiang, J.; Bi, C. Application of monitoring data, water pressure test and comprehensive geophysical method to identification of leakage of a core dam. *Water Resour. Hydropower Eng.* **2022**, *53*, 87–97. [CrossRef]

31. Zhang, W.B.; Shen, Z.Z.; Chen, G.Y.; Zhang, W.L.; Xu, L.Q.; Ren, J.; Wang, F. Optimization design and assessment of the effect of seepage control at reservoir sites under karst conditions: A case study in Anhui Province, China. *Hydrogeol. J.* **2021**, *29*, 1831–1855. [CrossRef]

32. Foyo, A.; Tomillo, C.; Maycotte, J.I.; Willis, P. Geological features, permeability and groutability characteristics of the Zimapan Dam Foundation, Hidalgo State, Mexico. *Eng. Geol.* **1997**, *46*, 157–174. [CrossRef]

33. Li, P.; Lu, W.X.; Long, Y.Q.; Yang, Z.P.; Li, J. Seepage analysis in a fractured rock mass: The upper reservoir of Pushihe pumped-storage power station in China. *Eng. Geol.* **2008**, *97*, 53–62. [CrossRef]

34. Berhane, G.; Walraevens, K. Geological challenges in constructing the proposed Geba dam site, northern Ethiopia. *Bull. Eng. Geol. Environ.* **2013**, *72*, 339–352. [CrossRef]

35. Barani, H.R.; Lashkaripour, G.; Ghafoori, M. Predictive permeability model of faults in crystalline rocks; verification by joint hydraulic factor (JH) obtained from water pressure tests. *J. Earth Syst. Sci.* **2014**, *123*, 1325–1334. [CrossRef]

36. Banks, D.; Odling, N.E.; Skarphagen, H.; RohrTorp, E. Permeability and stress in crystalline rocks. *Terra Nova* **1996**, *8*, 223–235. [CrossRef]

37. Manoutsoglou, E.; Lazos, I.; Steiakakis, E.; Vafeidis, A. The Geomorphological and Geological Structure of the Samaria Gorge, Crete, Greece-Geological Models Comprehensive Review and the Link with the Geomorphological Evolution. *Appl. Sci.* **2022**, *12*, 10670. [CrossRef]

38. Stober, I.; Bucher, K. Origin of salinity of deep groundwater in crystalline rocks. *Terra Nova* **1999**, *11*, 181–185. [CrossRef]

39. Roje-Bonacci, T.; Bonacci, O. The possible negative consequences of underground dam and reservoir construction and operation in coastal karst areas: An example of the hydro-electric power plant (HEPP) Ombla near Dubrovnik (Croatia). *Nat. Hazards Earth Syst. Sci.* **2013**, *13*, 2041–2052. [CrossRef]

40. Jemcov, I. Impact assessment of grout curtain on the hydraulic behavior in karst, based on time a series analysis. *Environ. Earth Sci.* **2019**, *78*, 415. [CrossRef]

41. Lu, M.; Wang, X.D.; Yue, F.J.; Liu, Z.H.; Shi, Z.Y.; Zhang, P. The effect of reservoir expansion from underground karst cave to surface reservoir on water quality in southwestern China. *Environ. Sci. Pollut. Res.* **2023**, *30*, 24718–24728. [CrossRef]